On the Development of Double Warm-Core Structures in Intense Tropical Cyclones

CHANH KIEU

Atmospheric Program, Department of Geological Sciences, Indiana University, Bloomington, Indiana

VIJAY TALLAPRAGADA

Environmental Modeling Center, NOAA/NWS/NCEP, College Park, Maryland

DA-LIN ZHANG

Department of Atmospheric and Oceanic Science, University of Maryland, College Park, College Park, Maryland

ZACHARY MOON

Atmospheric Program, Department of Geological Sciences, Indiana University, Bloomington, Indiana

(Manuscript received 8 January 2016, in final form 11 July 2016)

ABSTRACT

This study examines the formation of a double warm-core (DWC) structure in intense tropical cyclones (TCs) that was captured in almost all supertyphoon cases during the 2012–14 real-time typhoon forecasts in the northwestern Pacific basin with the Hurricane Weather Research and Forecasting Model (HWRF). By using an idealized configuration of HWRF to focus on the intrinsic mechanism of the DWC formation, it is shown that the development of DWC in intense TCs is accompanied by a thin inflow layer above the typical upper outflow layer. The development of this thin inflow layer in the lower stratosphere (~100–75 hPa), which is associated with an inward pressure gradient force induced by cooling at the cloud top, signifies intricate interaction of TCs with the lower stratosphere as TCs become sufficiently intense, which has not been examined previously. Specifically, it is demonstrated that a higher-level inflow can advect potentially warm air from the lower stratosphere toward the inner-core region, thus forming an upper-level warm core that is separated from a midlevel one of tropospheric air. Such formation of the upper-level warm anomaly in intense TCs is linked to an episode of intensification at the later stage of TC development. While these results are produced by HWRF, the persistent DWC and UIL features in all HWRF simulations of intense TCs suggest that the lower stratosphere may have significant impacts on the inner-core structures of intense TCs beyond the current framework of TCs with a single warm core.

1. Introduction

The tropical cyclone (TC) warm core, defined as a temperature anomaly between the TC eye region and the far-field environment, has been well known as a necessary condition to ensure a consistent TC dynamic and thermodynamic structure via the thermal wind relationship (e.g., Yanai 1964; Ooyama 1969; Liu et al. 1999; Schubert et al. 2007; Stern and Nolan 2012; Chen and Zhang 2013). Despite extensive studies of the TC warm core, the development of a double warm-core (DWC) configuration in which a midlevel warm core (MWC), located at z = 5–6 km, coexists with a higher-level warm core, located at z = 13–15 km (HWC) after TCs reach category 4 and above has not been fully acknowledged and examined.

Early observational studies by LaSeur and Hawkins (1963), Koteswaram (1967), Hawkins and Imbembo (1976), and Schwartz et al. (1996) are among the first to show the presence of DWC structures in a number of intense TCs, but their investigations were limited mostly within a general framework of describing overall TC structures with little understanding of the nature of DWCs. Figures 1a,b show an example of observed temperature profiles in the eyes of Hurricane Inez (1965) based on

Corresponding author address: Dr. Chanh Kieu, Department of Geological Sciences, Indiana University, 1001 10th Street, GY517 Atmospheric Science, Bloomington, IN 47405.
E-mail: ckieu@indiana.edu

DOI: 10.1175/JAS-D-16-0015.1

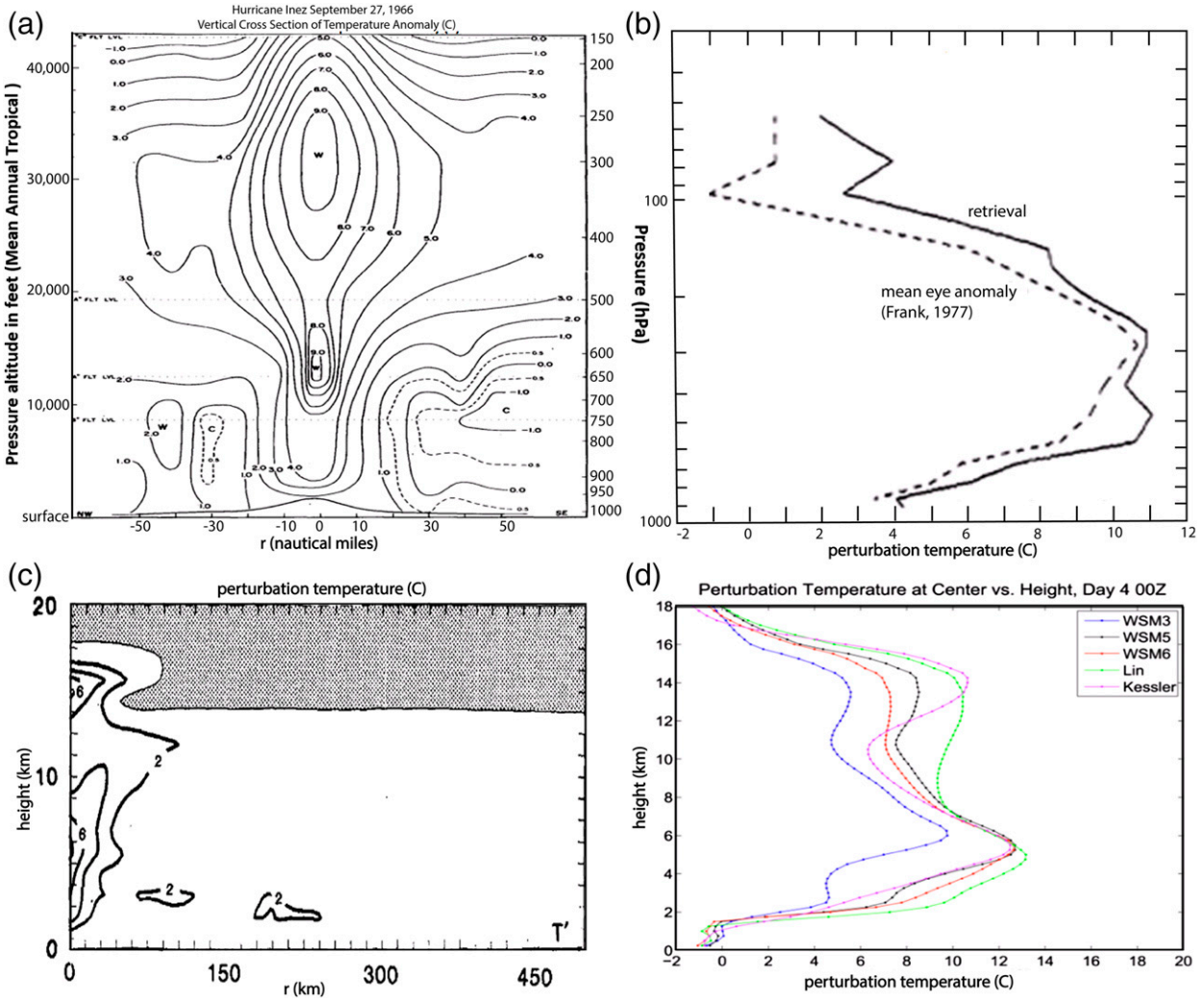

FIG. 1. (a) Vertical cross section through center of Hurricane Inez (1967) at its peak intensity (Hawkins and Imbembo 1976), (b) mean eye temperature anomalies retrieved from soundings shown by Schwartz et al. (1996), (c) radius–height cross section of temperature anomalies in an idealized simulation by RE87 (shading indicates the region with a temperature anomaly $< 0°C$), and (d) vertical profiles of the temperature anomalies in the inner-core region for different microphysics parameterization schemes—WSM3 (blue), WSM5 (black), WSM6 (red), Lin (green), and Kessler (purple)—from idealized simulations by Stern and Zhang (2013).

observations at four flight levels in the study of Hawkins and Imbembo (1976), and the eye-sounding retrieval for TC Oliver (1993) in Schwartz et al. (1996), in which DWCs occurred during the storms' peak intensity with an MWC around 550 hPa and an HWC near 250 hPa. A recent study by Durden (2013) has systematically examined more observed soundings in TC eyes, but the soundings were taken in the layers below 250 hPa, making it hard to investigate the DWC structure conclusively. Lack of observations of the DWC feature could be attributed to the fact that DWCs have appeared mainly in intense TC systems, in which direct upper-level observations were not always available.

In contrast, many cloud-permitting simulations of TCs frequently exhibit this DWC structure at the peak intensity of the TC development (e.g., Rotunno and Emanuel 1987, hereafter RE87; Stern and Nolan 2012; Wang and Wang 2014; Ohno and Satoh 2015). Figures 1c,d show examples of the model-simulated DWC structure in studies of RE87 and Stern and Zhang (2013), which are also seen in many different experiments with other models as well. It is intriguing that despite the abundant evidence of the DWC structure, these early studies focused only on the formation of the MWC, with little attention to the coexistence and conditions for both types of warm cores. An analysis of the inner-core dynamics by Stern and Nolan (2012) suggested that the MWC is an inherent thermal wind balanced characteristic of TCs, thus

rendering the roles of the HWC in determining TC intensity elusive.

Zhang and Chen (2012) and Chen and Zhang (2013) recently examined the generation of an HWC associated with the descending air of stratospheric origin, which coincided with the onset of rapid intensification of a record-breaking storm Hurricane Wilma (2005). This subsiding air was found to be the consequence of convective bursts within the radius of maximum wind (RMW). However, an analysis of the potential temperature budget equation for the inner-core region in a modeling study of Ohno and Satoh (2015) showed that the DWC structure at the mature stage in their idealized simulation is attributed to upper-level warming associated with the microphysics diabatic heating. By employing the Sawyer–Eliassen equation for further diagnostics, Ohno and Satoh (2015) suggested also that the forced subsidence at the upper vortex center is linked to the increased response of a secondary circulation to changes in the ambient static stability as the vortex extends into the lower stratosphere.

Given the lack of detailed inner-core observations for intense TCs, experimental real-time TC forecasts conducted by the U.S. National Centers for Environmental Prediction (NCEP) Environmental Modeling Center (EMC) during 2012–14 for the northwestern Pacific (WPAC) basin using the Hurricane Weather Research and Forecasting Model (HWRF) provide a unique opportunity to examine this type of DWC structure more systematically. In general, TCs in the WPAC basin experienced more often rapid intensification, larger storm sizes, and stronger intensity than those occurring over the other ocean basins, with an average of 4–5 supertyphoons each year (Knaff et al. 2014; Tallapragada et al. 2014). A recent report of the real-time performance of HWRF in the WPAC basin by Kieu and Tallapragada (2014) indeed documented two distinct common features of intense TCs in the WPAC area: (i) the existence of a persistent DWC structure at the peak intensity in a majority of intense TCs and (ii) a thin radial inflow layer right above the upper outflow layer associated with the DWC structure. Figure 2 shows an example of the HWRF 72-h forecast of temperature anomalies and radial flows for Supertyphoon Francisco (2013). One notices a distinct DWC structure, with a midlevel temperature anomaly of ~17 K around p = 500–400 hPa and another upper-level warm core of 11–12 K around p = 100 hPa, along with a thin upper-level inflow layer (UIL) near 75 hPa (Fig. 2b). Regardless of the model vortex initial conditions from cycle to cycle, such a DWC structure emerges once the model storm attains category 4 and stronger (i.e., the maximum

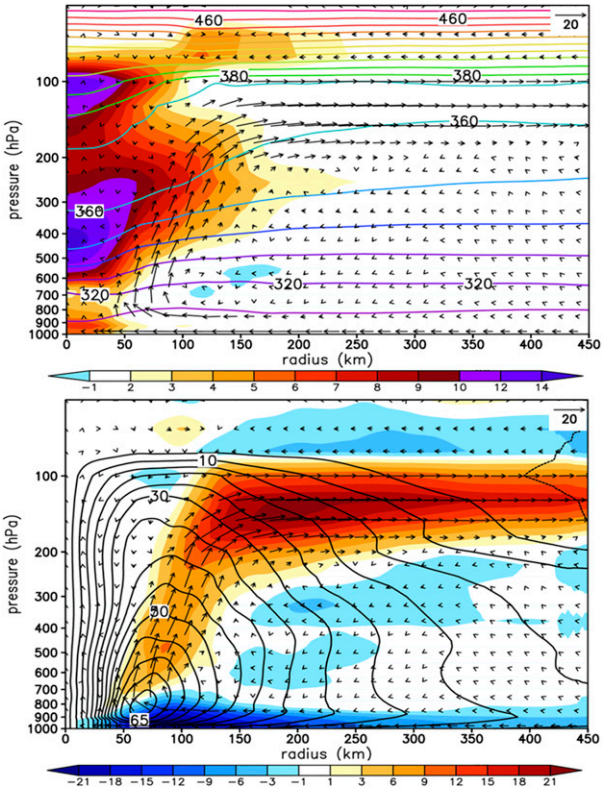

FIG. 2. Radial–height cross section of (a) temperature anomalies (color shaded, K) with respect to the far-field environment and the potential temperature (contoured at intervals of 10 K) and (b) radial flows (color shaded, m s^{-1}) and the tangential wind (contoured at an interval of 5 m s^{-1}) from the HWRF 18-h real-time forecast of Supertyphoon Francisco (2013), which is valid at 1200 UTC 20 Oct 2013 for the cycle initialized at 1200 UTC 17 Oct 2013. Superimposed on each panel are the in-plane flow vectors with the vertical motion multiplied by a factor of 5 (legend at bottom of each panel = 30 m s^{-1}).

10-m wind speed > 65 m s^{-1}) for more than 12 h in most supertyphoon cases. Of the 11 supertyphoons in 2012–14 that HWRF forecasted, 9 were found to possess a distinct DWC structure during their peak intensity stage (see Table 1 for a list of TCs with the DWC structure). The other two have a very brief period of strong intensity and so do not develop the DWC structure. The persistent development of DWCs in HWRF for these intense storms suggests some unknown physical mechanisms of TC development associated with strong rotation near the tropopause that we wish to investigate.

While modeling studies have captured the DWC structure in many idealized and real-data cases (e.g., Kieu and Tallapragada 2014; Ohno and Satoh 2015), whether DWCs are real features of intense TCs still remains a subject of further verification from observations. Given that the formation of a MWC is natural

TABLE 1. List of intense TCs during the 2012 and 2013 seasons in the northwestern Pacific Ocean basin and Indian Ocean Basin that the HWRF real-time forecasts captured the double warm-core structure. Winds are provided in knots (kt; 1 kt = 0.51 m s^{-1}).

No.	Year	Storm name (ID)	DWC captured	Maximum 10-m wind (kt) by JTWC	Period maintaining category 4 and above (h)
1	2012	Guchol (05W)	Missing cycles	130	36
2	2012	Bolaven (16W)	Yes	125	48
3	2012	Sanba (17W)	Yes	150	36
4	2012	Jelawat (18W)	Yes	140	102
5	2013	Phailin (02B)	Yes	140	42
6	2013	Soulik (07W)	Yes	125	24
7	2013	Utor (11W)	Yes	130	12
10	2013	Usagi (17W)	Yes	140	48
11	2013	Danas (23W)	No	125	12
12	2013	Francisco (26W)	Yes	140	66
13	2013	Lekima (28W)	Not clear–missing cycles	140	54
14	2013	Haiyan (31W)	Yes	170	66

from the TC-balanced dynamics, the questions of how the DWC structure forms, its connection to UIL, and its subsequent impacts on the TC development are of considerable importance to our understanding of TC processes. Because HWRF is tailored for TC forecasts with its physical processes and parameterization schemes well-tuned and extensively tested under various environmental conditions (Tallapragada et al. 2014; Gopalakrishnan et al. 2012), it is of interest to see how HWRF could produce the DWC structures in intense TCs and the associated mechanisms whereby they form. Thus, the objectives of this study are to (i) document the development of DWCs in an idealized simulation of a TC-like vortex using HWRF and (ii) examine the dynamics of an HWC in relation to UIL and the different dynamics involved between the HWC and MWC. With some successful rapid intensification forecasts of TCs over the WPAC basin by HWRF and its continuous improvement in providing better intensity forecasts (Tallapragada and Kieu 2014), it is reasonable to expect such a DWC configuration to be a true TC structure in an extreme intensity regime.

The next section describes the model configuration used to examine the DWC formation. Section 3 shows some specific conditions for the formation of a UIL from the quasi-balanced perspective. Section 4 presents a connection between the UIL and the formation of an HWC. Section 5 discusses differences between the HWC and MWC. A summary and concluding remarks are given in the final section.

2. Experiment descriptions

To systematically reproduce the DWC feature seen in the previous real-time forecasts of intense TCs in the WPAC basin, an idealized simulation is conducted herein using the latest version of HWRF (Tallapragada et al. 2014). The idealized model configuration is similar to that used in Gopalakrishnan et al. (2013) and Kieu et al. (2014) with triply nested domains on an f plane centered at 12.5°N and sea surface temperature fixed at 302 K. The model is initialized with the Jordan (1958) mean tropical sounding and a weak vortex that has the maximum surface azimuthal wind of 20 m s^{-1} and the RMW of 90 km in a quiescent environment. However, unlike the idealized configurations in the previous studies with 43 vertical levels, the simulation in this study has 61 vertical levels with the model top at 2 hPa instead of 50 hPa, and the three domains are configured at much higher horizontal resolutions of 8.1 km, 2.7 km, and 900 m, respectively. Such ultrahigh horizontal resolutions are used to allow for a better-resolved DWC feature inside the storm center. As discussed in section 1, DWCs appear in the TC eye and have a typical radius of 10–20 km. Therefore, high-resolution simulations are necessary to realistically capture the formation of detailed DWC structures in the inner-core region.

Model physics schemes used include the NCEP Global Forecasting System (GFS) planetary boundary layer (PBL) based on observational findings (Gopalakrishnan et al. 2012), improved Geophysical Fluid Dynamics Laboratory (GFDL) surface physics, improved Ferrier microphysics (Ferrier 1994), and implementation of the new GFS shallow convective parameterization. For the radiative parameterization, the newly implemented Rapid Radiative Transfer Model (RRTM-G) scheme for both the shortwave and longwave radiation parameterizations is used. While both the RRTM-G and the previous operational GFDL radiative parameterization schemes could capture a similar DWC development during the HWRF real-time experiments in 2012–14 (Tallapragada and Kieu 2014), the RRTM-G

radiation scheme allows for better representation of cloud-top cooling and cloud-base warming. Such an improved representation of the cloud-top cooling is important, because the cloud top is the place where TCs strongly interact with the lower stratosphere that we wish to focus on. One could in principle conduct sensitivity experiments with different radiative parameterization schemes to see how representative such radiative cooling at the cloud top is. Because of a limited number of radiation parameterization schemes in the current HWRF, we limit our experiments in this study only to the RRTM-G scheme due to its good representation of the cloud–radiation feedback as discussed in Bu et al. (2014). More details about all the other model features for the idealized configuration can be found in Gopalakrishnan et al. (2013).

Although idealized experiments contain some inherent issues related to either the lack of realistic asymmetries in the real atmosphere or uncertainties in representation of TC physical processes and feedbacks, such experiments have significant benefits for isolating the mechanisms of the DWC formation from other uncontrollable factors once DWC is reproduced. This is particularly relevant to the study of the DWC formation in this study, because rare upper-level observations of the TC inner-core region at high intensity regime make it difficult to understand details of the processes responsible for the formation of the DWC and to verify the model-simulated DWC development. It should be emphasized again that evidence of the DWC structure has been so far realized mostly for intense TCs. In practice, such a high-intensity phase does not last sufficiently long to send out reconnaissance flights for targeted observations (see Table 1 for typical durations of storms of category 4 and above in the WPAC basin). In this regard, idealized experiments are the only practical way to examine the TC inner-core processes above 100 hPa at the high intensity limit, despite potential caveats of idealized environmental conditions and simplifications.

As a first illustration, Fig. 3 shows the Hovmöller diagram of temperature anomalies at the eye center with respect to the far environment, and the evolution of the maximum 10-m wind along with the central pressure in a 5-day simulation. It is evident that while the formation of an MWC is natural and it persists in the 500–400-hPa layer throughout all stages of the TC development, the formation of an HWC is intermittent during the early phase of the storm development. The HWC becomes well defined only after the vortex intensity reaches 61 m s^{-1} at about 98 h into integration (cf. Figs. 3a,b). Of significance is that the emergence of the HWC is separate from the MWC, and its formation precedes a second

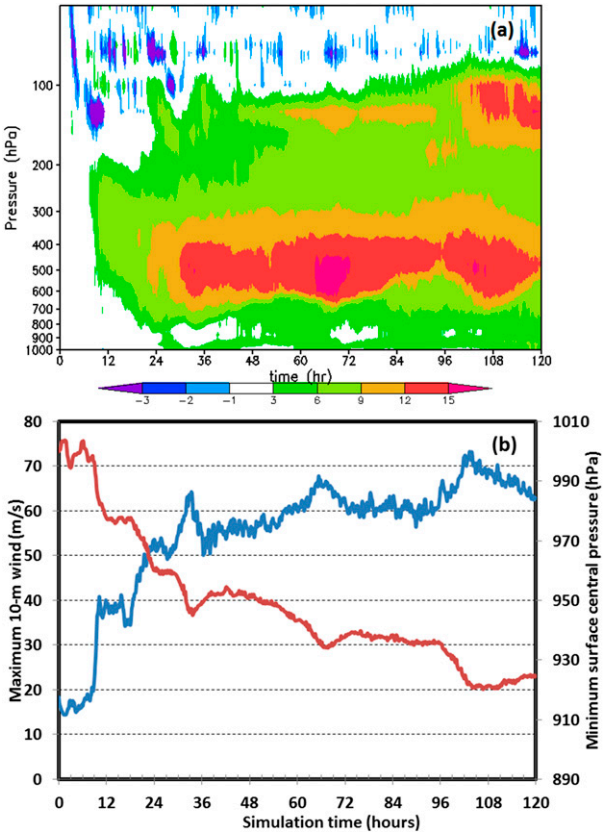

FIG. 3. (a) Hovmöller diagram of the temperature perturbation (color shaded, K) at the storm center from a 5-day idealized simulation with HWRF and (b) the corresponding maximum 10-m surface wind (blue, m s^{-1}) and the minimum sea level pressure (red, hPa) from the same 5-day simulation.

phase of intensification from 99 to 120 h when the model vortex already reaches a category-3 intensity. Such independent development of a warm-core structure is not specific to HWRF but can be seen also in recent analyses of temperature anomalies by Wang and Wang (2014) and Ohno and Satoh (2015). These results suggest that the development of an HWC is associated with the further intensification of an already intense storm. From this perspective, the Hovmöller diagram could illustrate the separate roles of the MWC and HWC during the TC development, particularly the emergence of the latter in conjunction with the associated intensification phase occurring after the storm reaches an intensity limit of ~61 m s^{-1}. More specific roles of the HWC and MWC during different stages of TC development are discussed in the next sections.

3. Development of the upper-level radial inflow

Given the persistent development of a UIL preceding the formation of an HWC in intense TCs as seen in the

HWRF's real-time forecasts of all supertyphoon cases, we first examine some necessary conditions for the formation of the UIL. Although previous high-resolution modeling studies have captured the development of UILs (e.g., Liu et al. 1999; Mrowiec et al. 2011; Chen and Zhang 2013), little has been discussed in the literature about the mechanisms whereby a UIL is generated. The lack of high-altitude observations renders the existence of a UIL difficult, if not impossible, to verify. A recent cloud-resolving study of Hurricane Wilma (2005) by Zhang and Chen (2012) shows the development of a UIL associated with multiple convective bursts in the TC eyewall, which is somewhat consistent with the convectively induced subsidence mechanism suggested by Shapiro and Willoughby (1982). Since HWRF repeatedly captures a UIL during the development of intense TCs, our aim here is to find specific TC structures that can support the formation of an UIL.

To lay out the general context of the UIL formation, Fig. 4 shows the radial flow at four different stages of the vortex development in our 900-m idealized experiment, which are 1-h averages centered at 18, 24, 36, and 72 h into the integration. While the UIL does not emerge before the tropical storm (TS) stage (Fig. 4a), it becomes noticeable after the model vortex attains the maximum surface wind of greater than 35 m s^{-1} (Figs. 4b–d). Specifically, the appearance of a UIL is persistent with a magnitude of 1–2 m s^{-1} right above the tropopause (~140 hPa), which extends all the way from the outer- to inner-core region. Such a UIL layer is present not only in the real-time configuration of 43 vertical levels and 50-hPa model top (Kieu and Tallapragada 2014), in idealized simulations with 61 vertical levels and 2-hPa model top, but also in all of the real-time forecasts of super typhoon cases in the WPAC basin. This indicates that the development of such a UIL may not be a simple model artifact, but related to some physical processes in the lower stratosphere that have not been fully examined.

To shed some light on the conditions for the formation of a UIL, we note that its existence implies that gradient wind balance is no longer valid, just like in the upper outflow and low-level inflow regions. Thus, it is necessary to establish conditions for a UIL from the quasi-balanced perspective such that the radial flow is permitted. In the log pressure cylindrical coordinates (r, z, λ) with z defined as

$$z = -H \ln\left(\frac{p}{p_s}\right), \tag{1}$$

where p_s is the surface pressure, the hydrostatic primitive equations system is given by

$$\frac{\partial u}{\partial t} + u\frac{\partial u}{\partial r} + w\frac{\partial u}{\partial z} - \frac{v^2}{r} = -\frac{\partial \Phi}{\partial r} + fv + F_u, \tag{2}$$

$$\frac{\partial v}{\partial t} + u\frac{\partial v}{\partial r} + w\frac{\partial v}{\partial z} + \frac{uv}{r} = -fu + F_v, \tag{3}$$

$$\frac{\partial \Phi}{\partial z} = \frac{RT}{H}, \tag{4}$$

$$\frac{1}{r}\frac{\partial (ur)}{\partial r} + \frac{\partial w}{\partial z} - Sw = 0, \quad \text{and} \tag{5}$$

$$\frac{\partial \theta}{\partial t} + u\frac{\partial \theta}{\partial r} + w\frac{\partial \theta}{\partial z} = Q + F_\theta, \tag{6}$$

where H is the coordinate scale height; (u, v, w) are axisymmetric wind components in the radial, azimuthal, and vertical directions, respectively; T is temperature; $F_{u,v}$ denote eddy frictional forcing; $S = (1/\rho)(\partial\rho/\partial z)$ is a stratification parameter; Φ is geopotential; Q is diabatic heating source/sink related to radiative transfer and phase transition; and F_θ is the diffusive term (Willoughby 1979). While our formulation in this quasi-balanced framework is for the strong intensity phase during which the axisymmetric approximations are most applicable, this framework does not take into account detailed physical processes related to diffusive forcings or cloud microphysics. Therefore, subtle processes such as strong downdrafts at the inner or outer edge of the eyewall cannot be modeled in this framework (see Liu et al. 1997, 1999). This issue is noteworthy because it later explains some deviations of the quasi-balanced flows from the model-simulated flows that are directly obtained from the model output as will be shown below.

Because the main focus here is on the conditions for the radial wind to change from outflow (i.e., $u > 0$) at lower levels to inflow at higher levels (i.e., $u < 0$), let us introduce a variable called vertical radial wind shear $\Gamma \equiv \partial u/\partial z$ that represents the rate of change of the radial flow with height. To illustrate the meaning of Γ, Fig. 5 shows the radius–height cross section of the radial inflow and the corresponding Γ valid at the 72 h into the integration. It is seen that Γ is mostly positive in the eyewall and peaks below the outflow level, indicating that the radial flow gradually changes from inflow within the PBL to outflow above the PBL. Above the outflow level, Γ becomes negative as the radial outflow decreases with height and turns into inflow in a layer from 100 to 50 hPa. Thus, any air parcel ascending along an absolute angular momentum (M) surface in the eyewall must experience a sign change in Γ from positive to negative if a UIL exists.

To examine the conditions for such a flip in the sign of Γ along M surfaces, let us take a z derivative of Eq. (2) as follows:

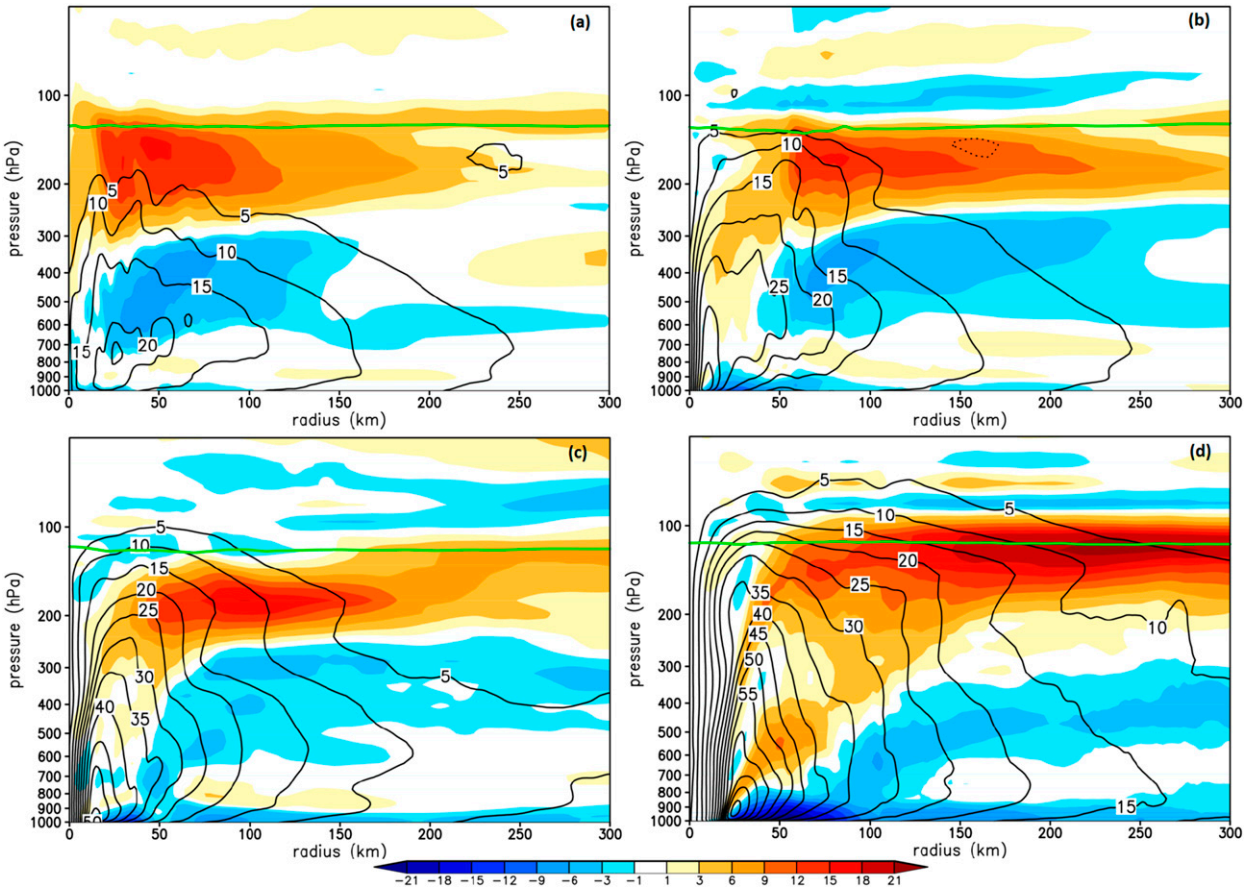

FIG. 4. Radius–height cross sections of the radial inflow (color shaded, m s^{-1}) and the tangential winds (contours at an interval of 5 m s^{-1}) at four different stages of the vortex development: (a) tropical storm stage valid at $t = 18$ h, (b) category 1 at $t = 24$ h, (c) category 4 at $t = 36$ h, and (d) category 5 at $t = 72$ h into the integration. They were obtained by averaging five consecutive outputs at 10-min intervals. The horizontal green lines denote the tropopause level.

$$\frac{\partial \Gamma}{\partial t} + u\frac{\partial \Gamma}{\partial r} + w\frac{\partial \Gamma}{\partial z} + \left(\frac{\partial u}{\partial r} + \frac{\partial w}{\partial z}\right)\Gamma = -\frac{\partial}{\partial r}\left(\frac{\partial \Phi}{\partial z}\right) + \left(f + \frac{2v}{r}\right)\frac{\partial v}{\partial z}, \tag{7}$$

where F_u in Eq. (2) is assumed to be negligible above the PBL. The neglect of F_u can be justified from Fig. 5, which shows that slantwise motion in the eyewall approximately follows M surfaces above the PBL—that is, the M-conserving flow as often assumed (see Emanuel 1986). The physical reason behind such an assumption follows from our simplified quasi-balanced model in Eqs. (1)–(5), in which frictional forcing is zero above the PBL, and the absolute angular momentum (AAM) has to be conserved. In full-physics model simulations, the eddy frictional forcing is small in the free atmosphere but the horizontal and vertical diffusion forcing are always present, which is why AAM is not absolutely conserved (Fig. 5b). This small forcing explains some tendency of the radial flows crossing the AAM surfaces as seen in Fig. 5a. Except for these small deviations, one could see that the overall secondary circulation and the M surfaces are fairly aligned, for which we will hereinafter assume for all trajectories inside the eyewall as in Emanuel (2003).

Using Eqs. (4) and (5), and following any M surface in the eyewall (e.g., any bold black contour in Fig. 5), Eq. (7) can be rewritten in Lagrangian form as follows:

$$\frac{D\Gamma}{Dt} + \left(Sw - \frac{u}{r}\right)\Gamma = -\frac{R}{H}\frac{\partial T}{\partial r} + \Omega\frac{\partial v}{\partial z}, \tag{8}$$

where $\Omega \equiv (f + 2v/r)$. Here, the total derivative $D\Gamma/Dt$ means that we follow a parcel along an M surface and compute Γ along a specific trajectory inside the eyewall. Integrating Eq. (8) for a parcel starting from the top of the PBL to the end of an M surface, and assuming the solution of Eq. (8) to be represented in the form,

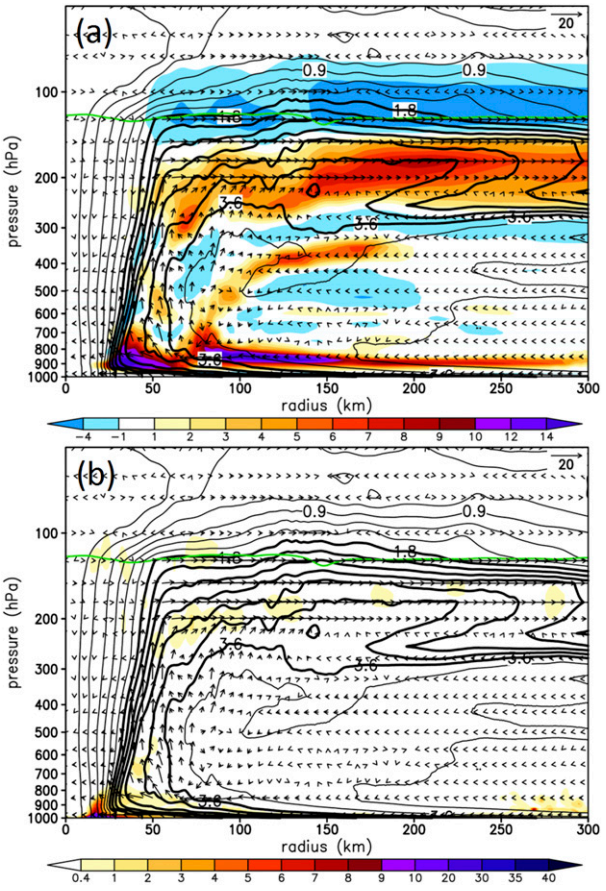

FIG. 5. As in Fig. 2, but for the change rate of the vertical shear of radial flows Γ (color shaded, $10^{-2}\,s^{-1}$), and the absolute angular momentum (contoured at an interval of $10^6\,m^2\,s^{-1}$), superimposed with in-plane flow vectors in the idealized experiment. Bolded contours denote the portion of the absolute angular momentum surfaces along the eyewall of the storm.

$$\Gamma(t) = \Gamma_0(t)e^{-\int[Sw-(u/r)]dt},$$

we obtain an expression for $\Gamma_0(t)$ as follows (see appendix A):

$$\Gamma_0(t) = \int\left(-\frac{R}{H}\frac{\partial T}{\partial r} + \Omega\frac{\partial v}{\partial z}\right)e^{\int_0^t[Sw-(u/r)]d\tau}\,dt + C, \qquad (9)$$

where C is an integral constant that represents contributions from the homogenous solution of Eq. (8), which can be determined from the initial condition of Γ. Since we integrate Eq. (8) along an M surface starting from the PBL top where the radial flow changes from strong inflow ($u < 0$) to weak outflow ($u > 0$), we can assume that the parcel always starts with $\Gamma(0) = 0$ such that $C = 0$ at the starting point. Note again that the technique of integration along an M surface is based critically on the assumption that an air parcel will conserve its absolute angular momentum along its trajectory such that the quasi-steady M surface at the mature stage can roughly represent the flow trajectory in the radius–height cross section. Provided that the frictional forcing in the free atmosphere is negligible, this assumption is reasonable and commonly used in previous TC-balanced models.

Because the exponential factor in the integrand does not change sign with time, the sign of $\Gamma(t)$ as the parcel ascends will be determined by the coefficient

$$A(t) \equiv -\frac{R}{H}\frac{\partial T}{\partial r} + \Omega\frac{\partial v}{\partial z}, \qquad (10)$$

which is essentially the imbalance of the thermal wind relationship when $A(t) \neq 0$. In the case of the exact thermal wind balance [i.e., $A(t) = 0$], any air parcel embedded in a balanced vortex is unable to change from inflow to outflow as it ascends, because $\Gamma(t)$ will preserve its sign during the entire trajectory. From this standpoint, the exact thermal wind balance can only be applied in the mid-troposphere where the secondary circulation is mostly in the vertical direction with little inflow or outflow to be consistent with $A(t) = 0$.

To highlight the role of each term in $A(t)$, Fig. 6 shows the radius–height cross section of each individual term on the right-hand side (rhs) of Eq. (10) and the total contribution $A(t)$. Note that the temperature gradient term $[-R/H(\partial T/\partial r)]$ is mostly positive in the core region owing to the existence of the warm core in the troposphere, whereas the vertical shear of the tangential flow $(\Omega\partial v/\partial z)$ is mainly negative as a result of the decrease of the tangential wind with height.[1] As expected, $A(t)$ flips sign from positive to negative along the M surfaces as an air parcel ascends in the eyewall, indicating that the outflow increases gradually with height and then changes to inflow aloft (Fig. 5). It should be mentioned that a simple sign change of $A(t)$ itself is not sufficient to determine the existence of the UIL, because $A(t) < 0$ may simply correspond to decrease of outflow with height. Note, however, that the UIL layer is above the outflow layer, and any condition that can lead to $A(t) < 0$ above the outflow layer could indeed suggest the formation of an UIL.

Given the significance of the thermal wind imbalance as indicated by the factor $A(t)$, we consider next a parcel starting at some point on an M surface above the PBL and then integrate Eq. (9) along the M surface. In this

[1] As long as the tangential wind is maximum at the surface and approaches zero near the tropopause, the term $\Omega\partial v/\partial z$ will be negative along any integrated trajectory on M surfaces in the eyewall region.

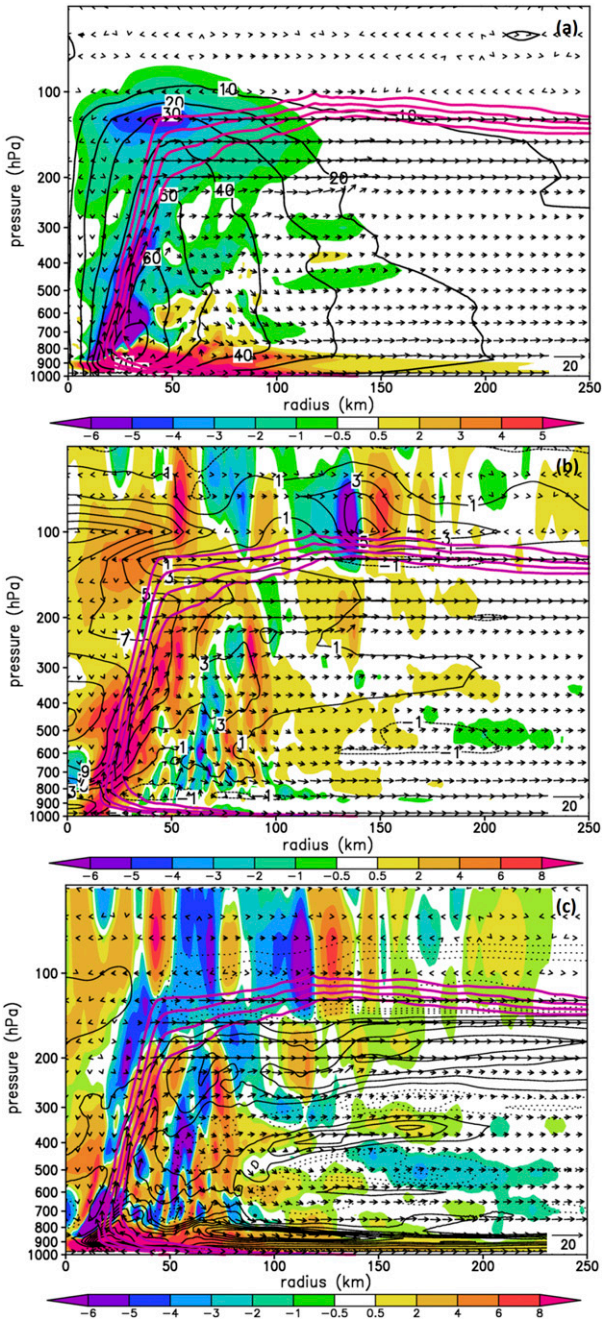

FIG. 6. As in Fig. 5, but for (a) $\Omega\partial v/\partial z$ [color shaded, $10^{-4}\,s^{-1}$, see Eq. (10)] and tangential wind speed (contoured at an of interval of $10\,m\,s^{-1}$), (b) $-(R/H)\partial T/\partial r$ [color shaded, $10^{-4}\,s^{-1}$, see Eq. (10)] and potential temperature anomalies (contoured at an interval of 2°C), and (c) the sum of (a) and (b) (color shaded, $10^{-4}\,s^{-1}$) and $\Gamma = \partial u/\partial z$ (contoured at an interval of $3\,m\,s^{-1}$). Solid (dotted) contours indicate the positive (negative) values. The red thick contours in all the panels indicate the M surfaces in the eyewall. The four thick red contours denote the AAM surfaces in the eyewall, which are set at 1.8, 2.1, 2.4, and $2.7 \times 10^6\,m^2\,s^{-1}$.

case, we obtain an interesting result that a parcel moving along a given M surface can turn from essentially vertical motion in the 800–300-hPa layer into an outflow in the 300–150-hPa layers (i.e., $\Gamma = \partial u/\partial z > 0$) only if $A(t) > 0$ at some points along the M surface. Indeed, since the parcel starts at the top of the PBL with $\Gamma(0) = 0$, $\Gamma(t)$ can turn positive at the outflow level only if there exists a domain on an M surface such that the integrand is positive; that is, $A(t) > 0$. Since $\Omega\partial v/\partial z$ is dominantly negative above the PBL, whereas $[-(R/H)\partial T/\partial r > 0]$ because of the presence of a warm core, the requirement of $A(t) > 0$ along an M surface amounts to the statement that an MWC must be located below the outflow layer so that the radial temperature gradient could dominate the shear term. As shown in Fig. 6c, $A(t)$ is indeed mostly positive above the PBL [except for some subtle area along the inner edge of the eyewall and related entrainment that the quasi-balance model in Eqs. (1)–(5) cannot describe], indicating that Γ becomes positive along the M surface. The positive region of $A(t)$ seen in Fig. 6c is consistent with the gradual change from radial inflow to outflow at higher levels. Were the thermal wind balance exact, the two terms on the rhs of Eq. (10) would be cancelled and there would be no change of the radial flow with height. Thus, the condition of $A(t) > 0$ in the eyewall shows that the gradient wind imbalance is required for the radial wind to change from inflow to outflow. This constraint explains the lower altitude of the balanced warm core as compared to that of the outflow layer—a fact that has not been explicitly stated from the previous studies (see Liu et al. 1999; Wang and Zhang 2003; Stern and Nolan 2012).

A second consequence from Eq. (9) is the required vortex structure that could support a UIL—that is, the sign of Γ changing from positive to negative above the upper outflow layer as shown in Fig. 3. Indeed, this sign change can only happen if a TC could possess a vertical structure such that $A(t)$ switches from positive to negative along M surfaces as air parcels ascend to even higher levels. Note that this condition on the TC structure is a necessary condition only; that is, if the radial flow changes from outflow near 150 hPa to inflow at ~75 hPa, then $A(t) < 0$ but not always vice versa, because it is possible that $A(t) < 0$ but $u > 0$ at this level, as mentioned earlier. Thus, the condition $A(t) < 0$ has to be supplied by a further requirement that the level at which an air parcel experiences this condition will be above the outflow level such as $A(t) < 0$ could suggest the development of the UIL. Since our main concern here is the constraint in the TC structure that could support the condition $A(t) < 0$, such a necessary condition suffices for us to examine the physical mechanism behind the development of an UIL.

Given that the tangential wind is generally decreasing with z in the storm central region (i.e., $r < 500$ km), there are two possibilities that allow $A(t) < 0$ to occur around $z = 75$ hPa at the strong intensity limit. The first possibility is the existence of a cold outer layer at the upper levels (with respect to the far-field environment) such that the radial temperature gradient in the outer region points inward as the air parcel ascends along an M surface; that is, $-(R/H)\partial T/\partial r < 0$. Because $\partial v/\partial z < 0$, the existence of such a cold layer aloft will ensure that $A(t) < 0$ as seen from Eq. (10). The development of an outer-core cold annulus may look ambiguous at first, but it is in fact similar to the necessary temperature gradient in the sea-breeze circulation. Indeed, a large canopy of the upper-level cloud overcast is acting more as a blackbody surface, which can absorb solar shortwave radiation effectively during the daytime,[2] but is cooled off quickly during the nighttime owing to longwave radiative cooling (Bu et al. 2014). In effect, the requirement of $-(R/H)\partial T/\partial r < 0$ can be satisfied if the cloud canopy cools faster than the ambient environment. This cooling leads to shrinkage of the atmospheric layer above the outflow layer, which results in an inward gradient of the pressure force. Of course radiative cooling is not the only factor that could ensure $-(R/H)\partial T/\partial r < 0$, but this condition would be most effectively met when significant radiative cooling occurs at the top of the TC outflow layer.

To demonstrate the development of such a cold upper layer above the outflow layer, Fig. 7 shows a sequence of upper-level cooling and its impact on the horizontal flows at 75 hPa at four different stages of the vortex development corresponding to each shown in Fig. 4. We can see the spreading of the coldest temperature area of ~217 K from $r = 200$ km at $t = 18$ h, to 500 km at $t = 48$ h, to about 800 km after $t = 72$ h. Of importance is that the cooling is peaked at the maximum intensity stage after long accumulation of the net radiative cooling during the course of integration (cf. Figs. 4 and 7c,d). The development of such an outer-core cold annulus is similar to that shown in the recent observational study by Dunion et al. (2014), who showed a variation of the cloud-top temperature associated with the diurnal cycle of convective pulses propagating from the inner core outward. The footprint of such outward spreading is the strong cooling above the outflow layer over an area of radius 200–600 km from the storm center (see Figs. 1 and 4 in Dunion et al. 2014), which is attributed partly to the radiative cooling after sunset (see also Fig. 11c for the net radiative cooling). While there are significant diurnal variations in the net radiative forcing, it is apparent that the cooling tendency is dominant, similar to that shown in Fig. 7, with the maximum cooling during the nighttime (see Bu et al. 2014) and that it justifies for the role of the radiative cooling in the outer-core region.

As a result of the strong cooling in the outer-core region, converging radial flows begin to develop above the upper outflow layer after the model vortex become sufficiently strong, which is opposite to an outflow at 100–150 hPa below. This is a direct consequence of the upper-level cold annulus that results in a low pressure at the inner-core region, thus allowing the pressure gradient force to point inward. The inward pressure gradient force is consistent with the development of negative geopotential height anomaly shown in Fig. 7 and the corresponding decrease of the area-averaged thickness of the 100–70-hPa layer within a radius of 300 km from the vortex center in Fig. 8. Apparently, there is a strong correlation between the upper-level cold temperature and the thickness of the 100–70-hPa layer during the entire course of simulation, with a signal of diurnal variation similar to that reported in Dunion et al. (2014). In this regard, the pressure gradient force is the forcing for the existence of the upper-level returning flows toward the storm center as seen in Figs. 4 and 7, allowing for an outer-core UIL to develop above the outflow layer seen in Fig. 5.

From the dynamical perspective, the required upper-level cold layer for the UIL development is physically expected. For intense TCs, only a small portion of eyewall updrafts with smaller M values at the inner edge of the eyewall can reach very high altitudes, entering the lower stratosphere, before turning outward (Emanuel 2003). Because of the small M values at the inner edge of the eyewall, this part of the updrafts tends to have the centrifugal force decreased rapidly as the flow turns outward at high levels. As a result, the radial pressure gradient force can dominate and push this flow back toward the center, leading to the formation of a UIL as seen in Figs. 4 and 7. Here, the dynamical force behind the formation of an UIL is the inward pressure gradient associated with a low anomaly in the storm central region, not simply a result of the continuity constraint. Thus, the cold outer annulus is important to ensure the condition $-R/H(\partial T/\partial r) < 0$ above the outflow level such that the inward pressure gradient force can exist for the UIL in the outer region. Note again that the change of sign of $A(t)$ along the M surface presented above by itself is not the explanation for the formation of UIL; the sign change is simply a manifestation of the existence of

[2] Since the emissivity of cloud is propositional to the cloud water optical depth, deep convective cloud is therefore very close to blackbody object (see Garrett et al. 2002).

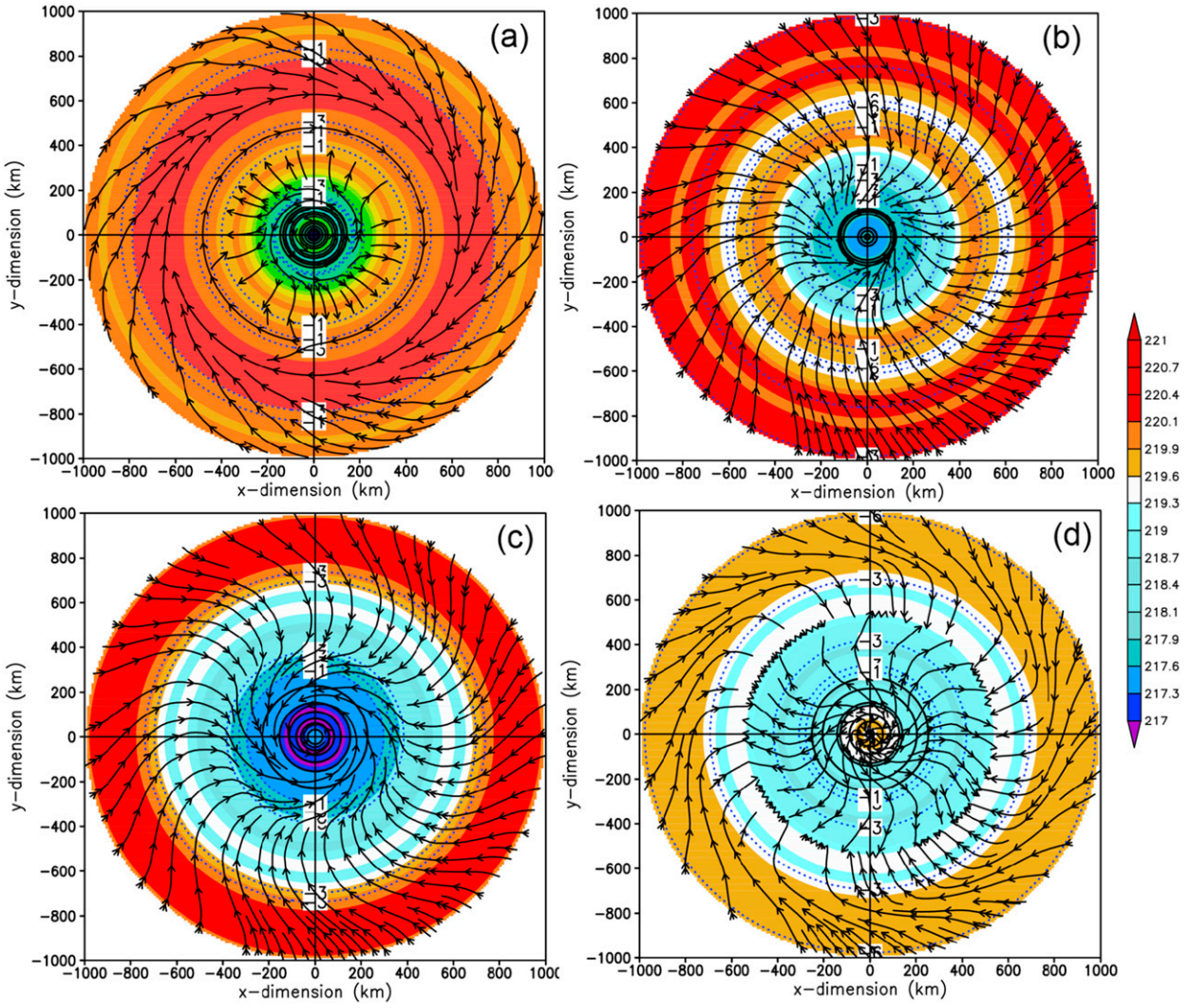

FIG. 7. Horizontal maps of the absolute temperature (color shaded, K) and streamlines at 75 hPa at four different stages of the vortex development from the idealized experiment: (a) $t = 18$, (b) $t = 24$, (c) $t = 48$, and (d) $t = 72$ h, which correspond to the radius–height cross sections in Fig. 4. Dotted contours are the geopotential height anomaly with respect to the environment at 1000 km from the storm center (at an interval of 10 m).

the outer cold annulus that gives rise to a TC structure for which $A(t) < 0$.

The second possibility for the condition $A(t) < 0$ to be met is the presence of a high-level warm ring in the storm central region once the eyewall convection is sufficiently strong to penetrate the tropopause. The returning subsidence on top of the eyewall can in fact lead to a warm ring that also produces a similar condition $-(R/H)\partial T/\partial r < 0$ inside the ring. While the cold annulus is mostly in the outer region, overshooting deep convection in the eyewall could effectively penetrate the tropopause, which is in turn decelerated and forced to return because of the strong stratification of the tropopause. Such impacts of the eyewall convection can be seen in Fig. 9, which shows a clear inner-core warm ring along with strong subsidence above the eyewall (around 75 hPa; see Fig. 9a). The presence of the local warm ring around 20–40-km radius shown in Fig. 9b is most apparent after the model vortex attains an intensity of $\sim 65\,\mathrm{m\,s^{-1}}$ (cf. Fig. 7d), thus generating a locally inward temperature gradient inside the upper-level warm ring (see Fig. 9). Like the cold annulus in the outer region, the inner-core warm ring also ensures the condition of $-(R/H)\partial T/\partial r < 0$. As a result, an inward pressure gradient force develops, accounting for the generation of the UIL in the eye (herein referred to as inner UIL to distinguish with the outer UIL associated with the cold annulus in the outer-core region). The consistency between the

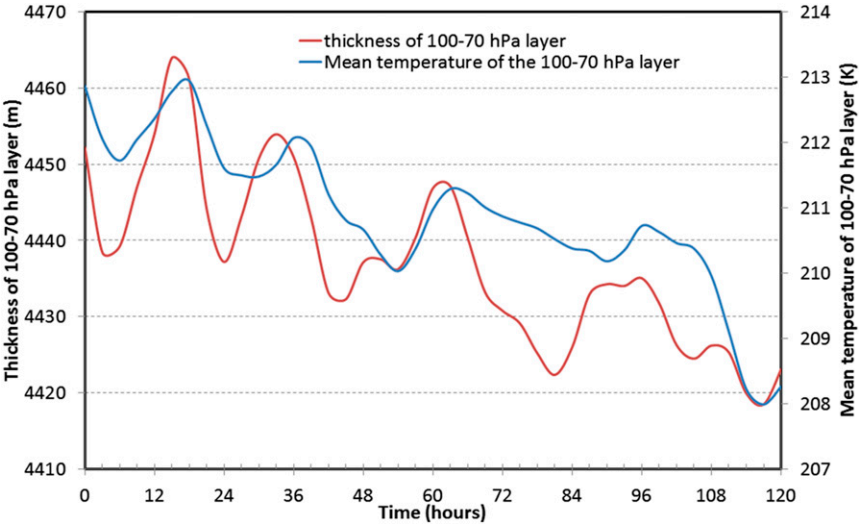

FIG. 8. Time series of the area-averaged thickness (red, m) of the 100–70-hPa layer over an area of 1000 km × 1000 km, and the corresponding mean temperature (blue, K) during the 5-day idealized simulation.

inner-core warm ring and the UIL above 100 hPa is nothing but a manifestation of the mass conservation according to which the vertical updraft inside the eyewall has to spread out as it reaches the tropopause with one branch returning to the eye, and the other branch follows the upper-level outflow (Shapiro and Willoughby 1982; Zhang and Chen 2012).

In addition to the aforementioned two possibilities related to either an outer-core cold annulus or an inner-core warm ring that could modify the radial temperature gradient at upper levels, it is also possible that evaporation or vertical diffusion of clouds at both the eyewall inner edge and on top of the cloud overcast can induce some penetrative downdrafts and further strengthen the UIL as discussed in Liu et al. (1999). Zhang et al. (2002) have indeed shown that the evaporative-driven downdrafts at the interface between the eyewall and eye may be another factor inducing the UIL inside the eye (see Fig. 2 therein). However, it is difficult to examine such subtle effects in the quasi-balanced framework presented in this study, as any moist physics mechanism would require detailed examination of the microphysics parameterization that the Lagrangian approach presented in this study could not afford. As will be seen further in section 4, the dominant role of the vertical advection of potential temperature appears to account for much of the warming in the eye, and we will therefore confine our analyses of the HWC within the framework of quasi-balanced flows only.

It should be stressed that the abovementioned favorable conditions for the UIL formation associated with the outer–core cold annulus or the inner-core warm ring are not limited to our idealized experiments or a specific configuration of HWRF. Both HWRF real-time experiments during the years 2012–14 years and recent upgrades of HWRF in 2015 with a new longwave radiative–cloud interaction scheme, more vertical levels (i.e., increased from 43 to 61 levels), and the model top as high as 2 hPa capture similar UIL development during our retrospective experiments of intense TCs (not shown). This is a good indication that the UIL development is not an artifact of the model top or any particular model configuration, but is a coherent structure of TC dynamics at the high intensity limit.

4. Formation of the upper-level warm core

The importance of an HWC in TC development was emphasized in a recent study by Zhang and Chen (2012), who showed that an upper warm core could account for more than 50% of the lower pressure at the surface. Before analyzing the connection of a UIL and formation of the DWC structure, let us briefly examine how effectively the formation of an HWC can lower the central surface pressure. This can be done by integrating the hydrostatic equation in the pseudoheight coordinate z from the surface to the top of the troposphere to obtain

$$\Phi(z=0) = \Phi|_{\text{top}} - \int_0^{\text{top}} \frac{RT(z)}{H}\,dz = \Phi|_{\text{top}} - \int_0^{\text{top}} \frac{R\overline{T}(z)}{H}\left[1+\frac{T'}{\overline{T}(z)}\right]dz, \qquad (11)$$

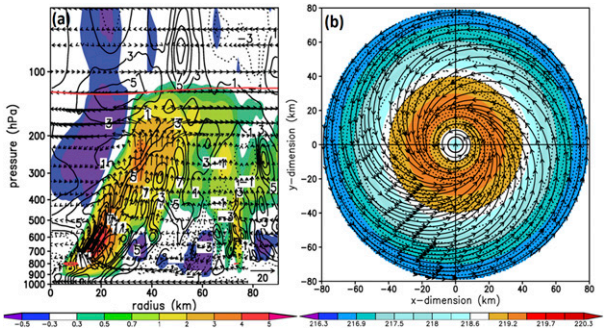

FIG. 9. (a) Radius–height cross section through the storm center of the vertical motion (color shaded, $m\,s^{-1}$), radial temperature gradient $-(R/H)\partial T/\partial r$ (contours with an interval of $2 \times 10^{-4}\,s^{-1}$), and the secondary circulation (vectors) and (b) horizontal cross section at 75 hPa of temperature (color shaded, K), vertical motion (subsidence) (dotted contours, $m\,s^{-1}$), and the corresponding streamlines from the 72-h integration.

where $\Phi|_{top}$ is the geopotential perturbation near the tropopause, T' is the temperature anomaly, and $\overline{T}(z)$ is the mean temperature profile. Apparently, given the same T', the higher the warm-core location, the larger the ratio $T'/\overline{T}(z)$ since $\overline{T}(z)$ decreases rapidly with height. As a result, the surface pressure is lower for higher-level warm-core perturbation. This demonstrates the efficacy of an HWC on enhancing the low pressure system once it appears (Fig. 11b).

Because of the importance of the HWC on TC late development, it is necessary to examine the role of a UIL in the formation of an HWC and subsequently the DWC structure. Although a UIL can develop as soon as the radial temperature gradient conditions above the outflow level are satisfied, the formation of the HWC depends further on the ability of the UIL to reach the vortex center and induce a warm anomaly at the upper levels. Figure 10 shows a series of the radius–height cross sections of temperature anomalies at four different stages of the storm life cycle that correspond to the UIL development in Fig. 4. It can be seen that below category-1 intensity (Figs. 10a,b), an upper warm core is not organized even with the existence of the UIL, mostly because there is no well-defined eye at the early stage (Fig. 4b). The HWC is more apparent when the UIL in the lower stratosphere approaches the storm inner-core region, which possesses a more organized eyewall and eye after the model vortex reaches category 2 (Fig. 10c). At the vortex mature stage, the HWC becomes most distinct, as shown in Figs. 7d and 10d, with a clear signal of the UIL aloft. This gross picture of the HWC formation suggests that the UIL plays a key role in generating warm advection from the lower stratosphere toward the storm center, thus forming an HWC at the strong intensity limit under favorable conditions discussed in section 3.

To quantitatively understand the role of the warm advection induced by the UIL in generating the HWC, Fig. 11 shows the potential temperature budget as defined by

$$\frac{\partial\theta}{\partial t} = -\left(u\frac{\partial\theta}{\partial r} + w\frac{\partial\theta}{\partial z}\right) + \mathrm{MP} + \mathrm{RAD},$$

where MP denotes contributions from the microphysics, diffusion, and the gravity drag terms and RAD represents the radiative forcing. Like in previous studies (e.g., Zhang et al. 2002; Ohno and Satoh 2015), Fig. 11 shows that the dominant forcings in the potential temperature budget at the time when the DWC is most apparent are largely due to the ADV $[\equiv -(u\partial\theta/\partial r + w\partial\theta/\partial r)]$ and the MP terms, which are opposite in sign but similar in magnitude below 200 hPa. Above 150 hPa where the impacts of moist physics and diffusion become rapidly diminished, the MP term is negligible as compared to the contribution from the advective forcing and radiative forcing. In particular, there exists a layer of warm advection toward the storm center right above the outflow layer, where the UIL is maximum, with significant warming of $\sim$1–2 $K\,h^{-1}$ (Fig. 11a). This advective warming is peaked in the eye of the vortex where the UIL starts to subside. Note that the upper-level inflow in the outer region is mostly along isentropic surfaces because of the presence of weak diabatic forcings. Thus, the impact of the UIL on inducing the HWC is most noticeable after the inflow enters the inner-core area and subsides, which is indicated by regions of significant warming tendency where it descends in the eye (Fig. 11a). In these regions, the condition for the UIL development [i.e., $-(R/H)\partial T/\partial r < 0$] is clearly met and the existence of the UIL is thus consistent with the convectively induced subsidence associated with the eyewall convection that penetrate across the tropopause (Shapiro and Willoughby 1982; Chen and Zhang 2013).

To further examine the relative impacts of the advective warming induced as the UIL subsides at the storm center, Fig. 12 exhibits horizontal maps of the ADV, MP, and RAD terms at $z = 100$ hPa right below the level of the UIL layer. Consistent with the dominant inflow at 75 hPa (Fig. 12) is the storm-scale subsidence in the inner-core region, which corresponds well to the dominant positive temperature advection (see dotted contours in Fig. 12d). Again, the ADV term is roughly two orders of magnitude larger than both the MP and the RAD terms, indicating the importance of the inner-core subsidence associated with the UIL. That the RAD term is much smaller than the other forcings indicates that the radiative cooling does not directly contribute to the formation of the HWC in the inner-core region but more or less to the development of the UIL via

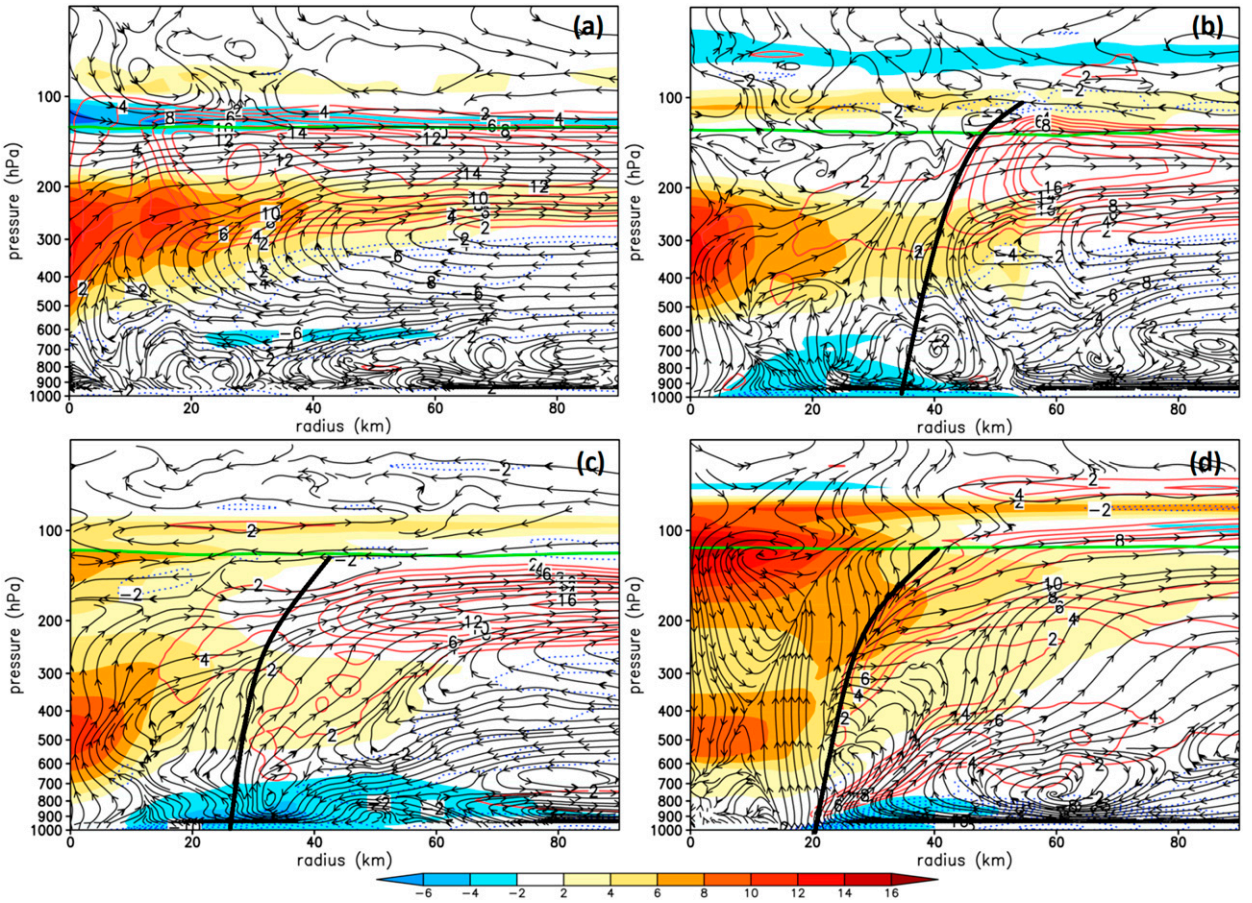

FIG. 10. As in Fig. 4, but for the temperature anomaly (color shaded, K) and the radial flow (contoured with an interval of 2 m s^{-1}). Superimposed also are streamlines of the secondary circulation. Solid (dotted) contours denote positive (negative) values.

persistent cooling in the outer-core region as discussed in section 3. Additional analysis of the ADV term confirms that the warming tendency in the inner-core region is associated mainly with the vertical advection (Fig. 13a), whereas the horizontal advection produces a ring of negative temperature tendency in the outer region as a result of the inward advection of the cold annulus as shown in Fig. 13b. Likewise, the dominant horizontal negative temperature tendency inside the eye is because the radial inflow tends to advect relatively colder air from outside toward a warmer core. Apparently, it is the strong descending motion associated with the UIL inside the eye that accounts for the largest warming tendency seen in Fig. 13a.

Since the descending motion is a key to the warming inside the TC eye during the formation of the HWC, it is important to note two different mechanisms for the development of the descending motion in the eye. The first mechanism is the convectively induced compensating subsidence, which is a result of the mass continuity (Zhang et al. 2000; Schubert et al. 2007). This kind of subsidence is confined near the inner edge of the eyewall, and so it is responsible more for the downdraft along the inner edge of the eyewall because of the limited radius of influence (Fig. 9b). The second mechanism, accounting for the weaker subsidence near the eye center, is more related to the dynamically induced pressure perturbation, which produces a downward gradient of the pressure perturbation forcing (Smith 1980; Zhang et al. 2000; Kieu and Zhang 2009. The essence of this mechanism is rooted in the fact that the pressure perturbation is proportional to the rotational winds; the stronger they are, the larger the central pressure deficit. Since the tangential wind decreases with height, the pressure deficit at lower levels will be larger than that at higher levels, thus producing a downward gradient force of pressure perturbations. From this perspective, the development of the warm core is consistent with the small residual between the downward pressure gradient force and buoyancy (Zhang et al. 2000).

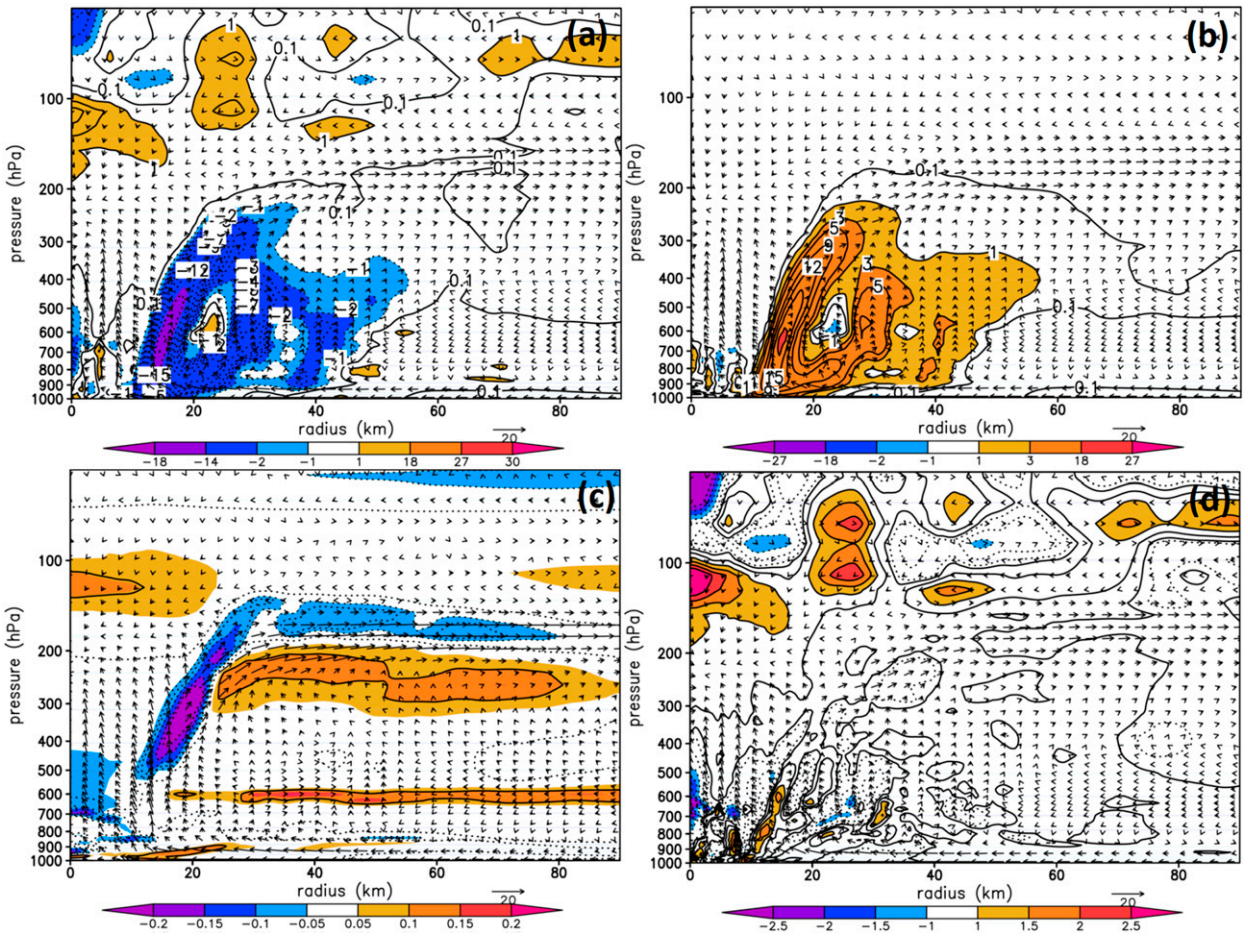

FIG. 11. Radius–height cross sections valid at $t = 108$ h for the heating rate associated with (a) the advective potential temperature (ADV, contoured at 0.1, 1, 3, 5, 9, 15, 21 K h^{-1}), (b) the microphysics and diffusion (MP) (contours, K h^{-1}), (c) shortwave and longwave radiation (RAD) (contours, K h^{-1}), and (d) total ADV + MP + RAD (contours, K h^{-1}). Color shaded areas in all the panels denote regions with heating rates greater than or less than 1 K h^{-1}. Superimposed is the corresponding in-plane secondary circulation (vectors, m s^{-1}).

Although the above analyses highlight the roles of the UIL in inducing the HWC at the strong intensity phase, we should note that it is not possible to draw conclusive inference about whether the HWC causes the model vortex to further strengthen or it is the strengthening of the model vortex that produces the HWC. Because of the diagnostic nature of our analysis, the most one can obtain from the budget equation is a strong connection between the UIL and the HWC, which suggests potential impacts of the lower stratosphere on the TC structure and development at the high intensity limit that is important to take into account. Indeed, if such impacts of the lower stratosphere on intense TCs are sufficiently effective, one would expect some statistical connection of the tropopause long-term variabilities and TC intensity, for which we will present in our upcoming study.

5. Double warm-core structure

While the development of an HWC depends on how effective the formation of the UIL is, the existence of an MWC is a must to ensure the dynamical consistency of the TC structure (Willoughby 1979; Kieu and Zhang 2009). The formation of the MWC has long been studied and often attributed to (i) the mechanically forced subsidence owing to the rapid rotation of the eyewall (Smith 1980; Zhang et al. 2000) and (ii) the convectively induced subsidence under the balanced constraint with a diabatic heat source in the eyewall (Shapiro and Willoughby 1982; Schubert et al. 2007; Zhang et al. 2000). Given the different origins and vertical distributions of the MWC and HWC at the different stages of TC development, they are expected to be governed by different processes.

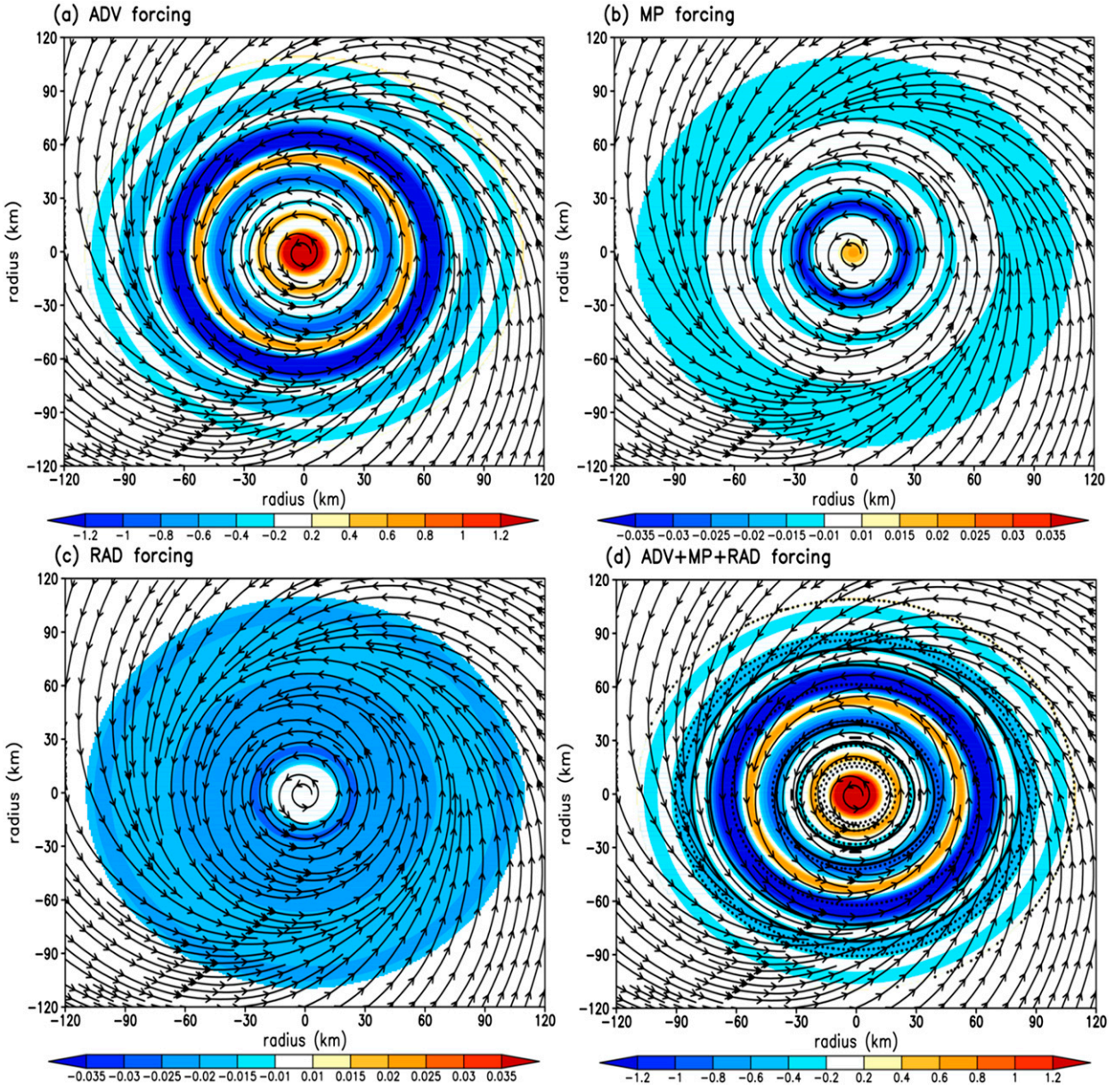

FIG. 12. Horizontal maps of the heating rate (color shaded, K h^{-1}) at 100 hPa associated with (a) ADV, (b) MP, (c) RAD, and (d) ADV + MP + RAD in the potential temperature budget equation, from 108-h integration. Superimposed are the horizontal flows at 75 hPa, showing a UIL above the outflow layer.

To understand the different nature of the HWC and MWC, we recall that the thermal wind balance is mostly valid between the PBL top and the upper outflow layer. Stern and Nolan (2012) pointed out that the height of the balanced MWC under this thermal wind relationship would be lower than what was often assumed in previous studies owing to the subtle dependence on the vertical shear of the squared tangential wind instead of the shear of the tangential wind. This can be seen directly from the thermal wind equation

$$\frac{R}{H}\frac{\partial T}{\partial r} = \Omega\frac{\partial v}{\partial z} \sim \frac{\partial}{\partial z}\left(\frac{v^2}{r}\right), \tag{12}$$

which gives the warm-core temperature anomaly $\Delta T(z)|_{r=0}$ as follows:

$$\Delta T(z)|_{r=0} \equiv T(r=0,z) - T(r=\infty,z) = -\int_0^\infty \frac{\partial}{\partial z}\left(\frac{v^2}{r}\right) dr. \tag{13}$$

So, $T\,(r = 0, z)$ will be maximized at $z = H$ such that

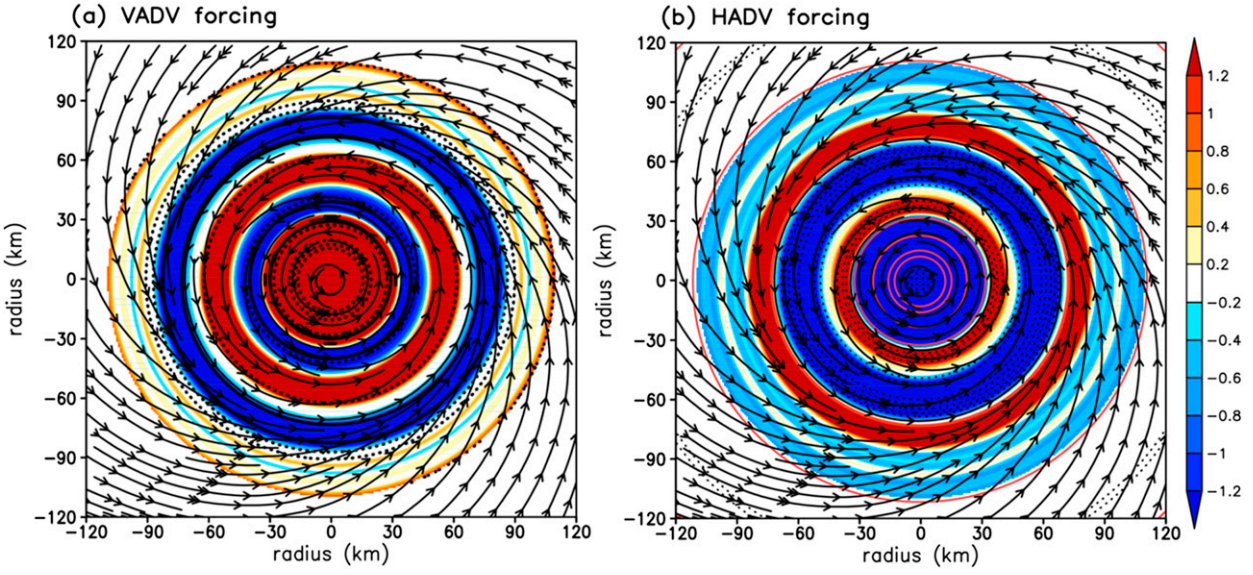

FIG. 13. As in Fig. 12, but for (a) vertical advection (color shaded, K h^{-1}) and vertical motion (dotted contours at −1, −0.5, −0.1, −0.01, 0.01, 0.1, 0.5, 1 m s^{-1}) and (b) horizontal advection (color shaded, K h^{-1}) and potential temperature (dotted contours at an interval of 0.3 K), which are superimposed with streamlines of the UIL.

$$\left.\frac{d\Delta T(z)}{dz}\right|_{z=H} = \frac{d}{dz}\left[\int_0^{\infty}\frac{\partial}{\partial z}\left(\frac{v^2}{r}\right)dr\right] = 0. \qquad (14)$$

Evidently, the height at which $\partial v/\partial z$ is maximized (i.e., $\partial^2 v/\partial z^2 = 0$) is not equal to the height at which the warm core is actually located at $z = H$, which is given approximately by the condition of $\partial^2(v^2/r)/\partial z^2 = 0$. Further calculation of (14) shows that H must be located at the level where $\partial^2 v/\partial z^2 < 0$ (i.e., below the location of the maximum vertical shear of tangential wind) and it is consistent with the MWC as discussed by Stern and Nolan (2012).

From the energetic perspective, both HWC and MWC are necessary for part of the potential energy (PE) to be converted to the TC kinetic energy [KE; see Tuleya and Kurihara (1975) and Hogsett and Zhang (2009)]. The efficacy of conversion from PE to KE is represented by the warm-core altitude and amplitude; that is, the higher altitude the warm core is or the warmer core would correspond to the lower mass gravitational center (see appendix B for variations of the vertical mass center of an air column with different heights of a warm core), and so is the larger KE that a TC can extract from the environment. Such importance of the warm core in affecting the TC kinetic energy can be justified directly from the energy budget equation if one recalls from the hydrostatic Eq. (11) that the pressure perturbation is proportional to the temperature anomaly. As such, a warmer temperature anomaly at the storm center would correspond to a lower central pressure, which consequently leads to larger kinetic energy [see Eq. (3) in Hogsett and Zhang for the connection between the kinetic energy tendency and the central pressure]. Viewing from this energy perspective, the UIL is a physical mechanism by which a warm core is built from the top downward, thus allowing the warm air in the lower stratosphere to be accumulated aloft at the storm center and further strengthen TCs. Although detailed analyses of the energy conversion associated with the HWC is not presented herein, potential contribution of the HWC to the TC development suggests that the interaction of the lower stratosphere and intense TC structure is an important mechanism in TC dynamics at the high intensity limit that should be further studied.

6. Concluding remarks

In this study, the development and implication of the DWC structure in intense TCs observed in both the HWRF real-time TC forecasts in the WPAC basin and the previous observational and modeling studies were examined. By analyzing the HWC structure in the upper layers where the thermal wind balance is generally not valid, we found an interesting constraint linking the development of a UIL to the imbalance in the thermal wind relationship. For sufficiently strong TCs, a UIL can develop within a thin upper layer in the lower stratosphere where the radial pressure gradient force induced by an inner-core warm ring or the cloud-top

cooling in the outer-core region eventually dominates the centrifugal force, thus pulling air toward the vortex center and forming the UIL. Once a TC eye is well defined at the mature stage, such a UIL in the lower stratosphere could advect warmer air toward the storm center and subsides, leading to formation of an HWC at the storm center.

Evaluation of the HWRF real-time forecasts for intense TCs in the WPAC basin during the 2012–14 experimental periods suggests a number of conditions for the development of a HWC in an 100–50-hPa layer including (i) the existence of cyclonic flow above 100 hPa, (ii) the existence of an inner-core warm ring related to strong overshooting convective bursts, and (iii) a warm tropopause with the potential temperature of greater than 370 K within the 100–50-hPa layer. Under these conditions, the HWC structure may develop and potentially trigger a further intensification of TCs. Note that the above conditions are obtained from strong TC cases (i.e., category 4 and above), and by no means conclusive or sufficient. A deeper question of proving that category 4 is an intensity limit above which the DWC could develop is however difficult to answer, as it requires a more complete theory of TC development beyond the scope of this work.

One aspect of the DWC formation presented herein that remains elusive is the sensitivity of the DWC structure to the radiative cooling at the cloud top. In a series of experiments with the Advanced Research version of WRF, Stern and Nolan (2012) showed that radiative forcing is generally small and should have negligible impact on the TC development at a time scale of several days. Their experiments with no radiative forcing in fact captured some signals of the DWC during the mature stage (see their Fig. 4), though the DWC is not as distinct as in the HWRF's model simulation. Our experiments with no radiation parameterization in HWRF show, however, a weaker vortex development (not shown), which seems to be consistent with the findings of Tang and Zhang (2016) that Hurricane Edouard (2016) could not even develop when the radiation parameterization is turned off. The fact that the DWC could manage to develop in experiments with no radiation parameterizations as in Stern and Nolan's study implies that the cloud-top cooling and the associated inward pressure gradient responsible for the formation of a UIL may be a function of more than just the radiative forcings for which this study could not fully answer.

Although idealized simulations in this study contain some caveats because of simplified environmental conditions and physics that are specific to HWRF, the results obtained herein have two significant implications with respect to the development of operational TC models and possible long-term variability of intense TCs. First, an HWC is potentially an important feature that should be taken into account during the model vortex initialization process so that the model can handle development of intense storms. While HWRF could capture well the RI phase of many intense TCs in WPAC during the real-time experiments from 2012 to 2014, we have noticed that HWRF still could not fully capture the magnitude of RI in several extreme cases such as Supertyphoon Francisco (2013), which underwent an RI from 40 to 55 m s^{-1} in just 6 h after the initialization time. If the presence of an HWC is necessary for such an extreme intensity, then any vortex initialization process must consider the DWC structure properly. Second, the importance of the HWC appears to depend critically on the ability of TCs to access the warm air above the tropopause. Such a linkage between the lower stratosphere and TCs at high intensity limit could indicate significant interaction between the intense TCs and the lower stratosphere. Better understanding of this TC–stratosphere interaction may therefore have important implication to future study of TC intensity variability for which we plan to investigate more thoroughly in our forthcoming study.

Acknowledgments. This work was supported by the Hurricane Forecasting Improvement Project (HFIP) of NOAA (Award NA16NWS4680026). DLZ was also supported by ONR Grant N000141410143 and NASA's Grant NNX12AJ78G. We thank three anonymous reviewers for their constructive comments and suggestions, which have substantially improved the presentation of this work.

APPENDIX A

Derivation of Eq. (9)

Consider first the homogeneous solution of Eq. (9), which is in the absence of the forcing on the rhs given by

$$\frac{D\Gamma}{Dt} + \left(Sw - \frac{u}{r}\right)\Gamma = 0. \tag{A1}$$

A particular solution of the homogeneous Eq. (A1) along a given flow trajectory can be found by directly integrate Eq. (A1) to obtain

$$\Gamma(t) = Ae^{-\int[Sw-(u/r)]dt}, \tag{A2}$$

where A is a constant. Note that because this is integration along a specific trajectory, all variables $S(t)$,

$u(t)$, $w(t)$, and $r(t)$ under the integrand in the solution (A2) are explicitly functions of time, which is specific to the selected trajectory.

Given the particular solution (A2) for the homogeneous Eq. (A1), the general solution for Eq. (9) can be finally obtained through a standard procedure by assuming the solution in the form

$$\Gamma(t) = \Gamma_0(t)e^{-\int[Sw-(u/r)]dt},$$

where $\Gamma_0(t)$ is now a function of time. Substitute this general solution into Eq. (8) and use of Eq. (A1), we have an equation for $\Gamma_0(t)$ as follows:

$$\frac{D\Gamma_0}{Dt} = \left(-\frac{R}{H}\frac{\partial T}{\partial r} + \Omega\frac{\partial v}{\partial z}\right)e^{\int[Sw-(u/r)]d\tau}. \quad \text{(A3)}$$

Equation (A3) can be integrated explicitly to obtain

$$\Gamma_0(t) = \int\left(-\frac{R}{H}\frac{\partial T}{\partial r} + \Omega\frac{\partial v}{\partial z}\right)e^{\int_0^t[Sw-(u/r)]d\tau}\,dt + C, \quad \text{(A4)}$$

which is the solution (9) given in the text.

APPENDIX B

Effect of Warm Cores on Lowering the Gravitational Center of a Vertical Column

In this appendix, we show that a gravitational center of an air column with a higher-level warm core is lower than that associated with a lower-level warm core. This can be seen by comparing the mass centers for two different air columns: one with a warm column and the other with a cold column at the upper level. Assuming that the density of the warm column is less than the cold column by an amount δ[i.e., $\rho_w(z) = \rho_c(z) - \delta(z)$], the centers of mass of the warm and the cold columns are

$$\overline{z}_c = \frac{\int z\rho_c\,dz}{\int \rho_c\,dz} \quad \text{(B1)}$$

and

$$\overline{z}_w = \frac{\int z\rho_w\,dz}{\int \rho_w\,dz}, \quad \text{(B2)}$$

respectively. Substituting $\rho_w(z) = \rho_c(z) - \delta(z)$ into Eq. (A2) gives

$$\begin{aligned}\overline{z}_w &= \frac{\int z[\rho_c(z)-\delta(z)]\,dz}{\int[\rho_c(z)-\delta(z)]\,dz}\\ &\approx \frac{\int z\rho_c\,dz}{\int\rho_c\,dz}\left[1-\frac{\int z\delta(z)\,dz}{\int z\rho_c\,dz}+\frac{\int\delta(z)\,dz}{\int\rho_c\,dz}\right]\\ &= \overline{z}_c\left[1-\frac{\int(z-\overline{z}_c)\delta(z)\,dz}{\overline{z}_c\int\rho_c\,dz}\right], \quad \text{(B3)}\end{aligned}$$

in which the Taylor series expansion has been used in going from step 1 and step 2. Since $\delta(z)$ is different from zero for $z > \overline{z}_c$ because of the assumed upper-level warm column, the integration on the right-hand side of Eq. (A3) will be positive, and therefore $\overline{z}_w < \overline{z}_c$. This demonstrates that the development of an upper-level warm core will lower the mass center of TCs, thus allowing for more potential energy to be converted to kinetic energy. An analogous situation that can also lower the TC mass center is the development of a cold core at the lower level for which Eq. (A3) will also give $\overline{z}_w < \overline{z}_c$.

REFERENCES

Bu, Y. P., R. G. Fovell, and K. L. Corbosiero, 2014: Influence of cloud–radiative forcing on tropical cyclone structure. *J. Atmos. Sci.*, **71**, 1644–1662, doi:10.1175/JAS-D-13-0265.1.

Chen, H., and D.-L. Zhang, 2013: On the rapid intensification of Hurricane Wilma (2005). Part II: Convective bursts and the upper-level warm core. *J. Atmos. Sci.*, **70**, 146–172, doi:10.1175/JAS-D-12-062.1.

Dunion, J. P., C. D. Thorncroft, and C. S. Velden, 2014: The tropical cyclone diurnal cycle of mature hurricanes. *Mon. Wea. Rev.*, **142**, 3900–3919, doi:10.1175/MWR-D-13-00191.1.

Durden, S. L., 2013: Observed tropical cyclone eye thermal anomaly profiles extending above 300 hPa. *Mon. Wea. Rev.*, **141**, 4256–4268, doi:10.1175/MWR-D-13-00021.1.

Emanuel, K. A., 1986: An air-sea interaction theory for tropical cyclones. Part I: Steady-state maintenance. *J. Atmos. Sci.*, **43**, 585–604, doi:10.1175/1520-0469(1986)043<0585:AASITF>2.0.CO;2.

——, 2003: Tropical cyclones. *Annu. Rev. Earth Planet. Sci.*, **31**, 75–104, doi:10.1146/annurev.earth.31.100901.141259.

Ferrier, B. S., 1994: A double-moment multiple-phase four-class bulk ice scheme. Part I: Description. *J. Atmos. Sci.*, **51**, 249–280, doi:10.1175/1520-0469(1994)051<0249:ADMMPF>2.0.CO;2.

Frank, W. M., 1977: The structure and energetics of the tropical cyclone I. Storm structure. *Mon. Wea. Rev.*, **105**. 1119–1135, doi:10.1175/1520-0493(1977)105<1119:TSAEOT>2.0.CO;2.

Garrett, T. J., L. F. Radke, and P. V. Hobbs, 2002: Aerosol effects on cloud emissivity and surface longwave heating in the Arctic. *J. Atmos. Sci.*, **59**, 769–778, doi:10.1175/1520-0469(2002)059<0769:AEOCEA>2.0.CO;2.

Gopalakrishnan, S., and Coauthors, 2012: Hurricane Weather Research and Forecasting (HWRF) model: 2012 scientific documentation.

NCAR Development Tested Bed Center Rep., 96 pp. [Available online at http://www.dtcenter.org/HurrWRF/users/docs/scientific_documents/HWRFScientificDocumentation_v3.4a.pdf.]

——, F. Marks, J. A. Zhang, X. Zhang, J.-W. Bao, and V. Tallapragada, 2013: A study of the impacts of vertical diffusion on the structure and intensity of the tropical cyclones using the high-resolution HWRF system. *J. Atmos. Sci.*, **70**, 524–541, doi:10.1175/JAS-D-11-0340.1.

Hawkins, H. F., and S. M. Imbembo, 1976: The structure of a small, intense hurricane—Inez 1966. *Mon. Wea. Rev.*, **104**, 418–442, doi:10.1175/1520-0493(1976)104<0418:TSOASI>2.0.CO;2.

Hogsett, W., and D.-L. Zhang, 2009: Numerical simulation of Hurricane Bonnie (1998). Part III: Energetics. *J. Atmos. Sci.*, **66**, 2678–2696, doi:10.1175/2009JAS3087.1.

Jordan, C. L., 1958: Mean soundings for the West Indies area. *J. Meteor.*, **15**, 91–97, doi:10.1175/1520-0469(1958)015<0091:MSFTWI>2.0.CO;2.

Kieu, C. Q., and D.-L. Zhang, 2009: An analytical model for the rapid intensification for tropical cyclones. *Quart. J. Roy. Meteor. Soc.*, **135**, 1336–1349, doi:10.1002/qj.433.

——, and V. Tallapragada, 2014: On the development of double warm cores in intense tropical cyclones in the HWRF model. *31st Conf. on Hurricanes and Tropical Meteorology*, San Diego, CA, Amer. Meteor. Soc., 17D.4. [Available online at https://ams.confex.com/ams/31Hurr/webprogram/Paper243675.html.]

——, ——, and W. Hogsett, 2014: Vertical structure of tropical cyclones at onset of the rapid intensification in the HWRF model. *Geophys. Res. Lett.*, **41**, 3298–3306, doi:10.1002/2014GL059584.

Knaff, J., S. Longmore, and D. Molenar, 2014: An objective satellite-based tropical cyclone size climatology. *J. Climate*, **27**, 455–476, doi:10.1175/JCLI-D-13-00096.1.

Koteswaram, P., 1967: On the structure of hurricanes in the upper troposphere and lower stratosphere. *Mon. Wea. Rev.*, **95**, 541–564, doi:10.1175/1520-0493(1967)095<0541:OTSOHI>2.3.CO;2.

LaSeur, N. E., and H. F. Hawkins, 1963: An analysis of Hurricane Cleo (1958) based on data from research reconnaissance aircraft. *Mon. Wea. Rev.*, **91**, 694–709, doi:10.1175/1520-0493(1963)091<0694:AAOHCB>2.3.CO;2.

Liu, Y., D.-L. Zhang, and M. K. Yau, 1997: A multiscale numerical study of Hurricane Andrew (1992). Part I: Explicit simulation and verification. *Mon. Wea. Rev.*, **125**, 3073–3093, doi:10.1175/1520-0493(1997)125<3073:AMNSOH>2.0.CO;2.

——, ——, and ——, 1999: A multiscale numerical study of Hurricane Andrew (1992). Part II: Kinematics and inner-core structures. *Mon. Wea. Rev.*, **127**, 2597–2616, doi:10.1175/1520-0493(1999)127<2597:AMNSOH>2.0.CO;2.

Mrowiec, A. A., S. T. Garner, and O. M. Pauluis, 2011: Axisymmetric hurricane in a dry atmosphere: Theoretical framework and numerical experiments. *J. Atmos. Sci.*, **68**, 1607–1619, doi:10.1175/2011JAS3639.1.

Ohno, T., and M. Satoh, 2015: On the warm core of a tropical cyclone formed near the tropopause. *J. Atmos. Sci.*, **72**, 551–571, doi:10.1175/JAS-D-14-0078.1.

Ooyama, K., 1969: Numerical simulation of the life cycle of tropical cyclones. *J. Atmos. Sci.*, **26**, 3–40, doi:10.1175/1520-0469(1969)026<0003:NSOTLC>2.0.CO;2.

Rotunno, R., and K. A. Emanuel, 1987: An air–sea interaction theory for tropical cyclones. Part II: Evolutionary study using a nonhydrostatic axisymmetric numerical model. *J. Atmos. Sci.*, **44**, 542–561, doi:10.1175/1520-0469(1987)044<0542:AAITFT>2.0.CO;2.

Schubert, W. H., C. M. Rozoff, J. L. Vigh, B. D. McNoldy, and J. P. Kossin, 2007: On the distribution of subsidence in the hurricane eye. *Quart. J. Roy. Meteor. Soc.*, **133**, 595–605, doi:10.1002/qj.49.

Schwartz, M. J., J. W. Barrett, P. W. Fieguth, P. W. Rosenkranz, M. S. Spina, and D. H. Staelin, 1996: Observations of thermal and precipitation structure in a tropical cyclone by means of passive microwave imagery near 118 GHz. *J. Appl. Meteor.*, **35**, 671–678, doi:10.1175/1520-0450(1996)035<0671:OOTAPS>2.0.CO;2.

Shapiro, L. J., and H. E. Willoughby, 1982: The response of balanced hurricanes to local sources of heat and momentum. *J. Atmos. Sci.*, **39**, 378–394, doi:10.1175/1520-0469(1982)039<0378:TROBHT>2.0.CO;2.

Smith, R. K., 1980: Tropical cyclone eye dynamics. *J. Atmos. Sci.*, **37**, 1227–1232, doi:10.1175/1520-0469(1980)037<1227:TCED>2.0.CO;2.

Stern, D. P., and D. S. Nolan, 2012: On the height of the warm core in tropical cyclones. *J. Atmos. Sci.*, **69**, 1657–1680, doi:10.1175/JAS-D-11-010.1.

——, and F. Zhang, 2013: How does the eye warm? Part I: A potential temperature budget analysis of an idealized tropical cyclone. *J. Atmos. Sci.*, **70**, 73–90, doi:10.1175/JAS-D-11-0329.1.

Tallapragada, V., and C. Q. Kieu, 2014: Real-time forecasts of typhoon rapid intensification in the North Western Pacific basin with the NCEP operational HWRF model. *Trop. Cyclone Res. Rev.*, **3**, 63–77.

——, ——, Y. Kwon, S. Trahan, Q. Liu, Z. Zhang, and I.-H. Kwon, 2014: Evaluation of storm structure from the operational HWRF during 2012 implementation. *Mon. Wea. Rev.*, **142**, 4308–4325, doi:10.1175/MWR-D-13-00010.1.

Tang, X., and F. Zhang, 2016: Impacts of the diurnal radiation cycle on the formation, intensity, and structure of Hurricane Edouard (2014). *J. Atmos. Sci.*, **73**, 2871–2892, doi:10.1175/JAS-D-15-0283.1.

Tuleya, R. E., and Y. Kurihara, 1975: The energy and angular momentum budgets of a three-dimensional tropical cyclone model. *J. Atmos. Sci.*, **32**, 287–301, doi:10.1175/1520-0469(1975)032<0287:TEAAMB>2.0.CO;2.

Wang, H., and Y. Wang, 2014: A numerical study of Typhoon Megi (2010). Part I: Rapid intensification. *Mon. Wea. Rev.*, **142**, 29–48, doi:10.1175/MWR-D-13-00070.1.

Wang, X., and D.-L. Zhang, 2003: Potential vorticity diagnosis of a simulated hurricane. Part I: Formulation and quasi-balanced flow. *J. Atmos. Sci.*, **60**, 1593–1607, doi:10.1175/2999.1.

Willoughby, H. E., 1979: Forced secondary circulations in hurricanes. *J. Geophys. Res.*, **84**, 3173–3183, doi:10.1029/JC084iC06p03173.

Yanai, M., 1964: Formation of tropical cyclones. *Rev. Geophys.*, **2**, 367–414, doi:10.1029/RG002i002p00367.

Zhang, D.-L., and H. Chen, 2012: Importance of the upper-level warm core in the rapid intensification of a tropical cyclone. *Geophys. Res. Lett.*, **39**, L02806, doi:10.1029/2012GL052355.

——, Y. Liu, and M. K. Yau, 2000: A multiscale numerical study of Hurricane Andrew (1992). Part III: Dynamically induced vertical motion. *Mon. Wea. Rev.*, **128**, 3772–3788, doi:10.1175/1520-0493(2001)129<3772:AMNSOH>2.0.CO;2.

——, ——, and ——, 2002: A multiscale numerical study of Hurricane Andrew (1992). Part V: Inner-core thermodynamics. *Mon. Wea. Rev.*, **130**, 2745–2763, doi:10.1175/1520-0493(2002)130<2745:AMNSOH>2.0.CO;2.